Robust Superhydrophobicity in Large-Area Nanostructured Surfaces Defined by Block-Copolymer Self Assembly

Antonio Checco, Atikur Rahman, and Charles T. Black**

Many natural surfaces such as plant leaves,[1] insects,[2] and animal bodies[3] are superhydrophobic (SH), with a water contact angle in excess of 150° and contact-angle hysteresis (defined as the difference between advancing and receding angles) smaller than 5°. Several studies have suggested that combinations of hydrophobic surface chemistry (contact angle > 90°) and surface texture are responsible for the observed superhydrophobic properties.[4–6] These findings are rationalized by the Cassie–Baxter (CB) model,[7] where air bubbles trapped in the hydrophobic texture reduce (increase) the area fraction of the solid/liquid (liquid/air) interface, thereby enhancing the hydrophobicity and the droplet's ability to roll off the surface. However, this "Cassie–Baxter state" is metastable because the liquid/air interface above the rough solid can sustain only a finite pressure, which scales approximately as γ/d, where γ denotes the water surface tension and d is the characteristic size of the surface texture.[8–11] A liquid subjected to an external pressure in excess of the critical value (either hydrostatic pressure or dynamic pressure caused by, for example, a droplet impact) infiltrates the texture, resulting in irreversible loss of superhydrophobic properties[12]. For example, a millimeter-sized raindrop falling at a terminal velocity of ca. 1 m s^{-1} has sufficient kinetic energy to penetrate a SH surface with micrometer-size texture upon impact.[8,10,13] For this reason, it has been argued that a defining characteristic of SH surfaces is their ability to completely repel impinging drops,[14] in addition to having a large contact angle and small hysteresis.

Robust SH surfaces resist forced infiltration, requiring higher critical pressures before breaking down. Some natural surfaces exhibit hierarchical textures at both micrometer and sub-micrometer length scales in order to achieve enhanced and robust water repellency.[15,16] However, the specific roles of nano- and micro-textures in optimizing SH behavior in both static and dynamic conditions remain matter of debate.[17,18] Indeed, previous studies have shown that nanoscale features alone can achieve similar static contact angles and contact angle hysteresis compared with hierarchical surfaces.[19–21]

In particular, surfaces textured at the sub-100 nm length scale may achieve the robustness required for applications such as automotive and aircraft windshields, and steam turbine power generators, where fluids are subjected to high pressures or when droplets impact solid surfaces at speeds in excess of 10 m s^{-1}. They may also enable integration of SH coatings with antifouling and low flow-resistance into nanofluidic devices.[22] Patterning surfaces at nanoscale dimensions with accompanying control over the aspect ratio and geometry of the texture features provides an opportunity for both fundamental and applied research on surfaces with special wettability. Well-defined nanoscale texture geometries can enable studies of liquid infiltration into model hydrophobic nanostructures[23] in order to elucidate the role of nanotextures in stabilizing the SH properties. In turn, such fundamental understanding will facilitate rational design of highly robust SH surfaces.

Previous approaches to creating these types of nanostructured surfaces have employed optical lithography,[21] chemical vapor deposition,[19] and maskless deep reactive ion etching.[20] However, achieving well-defined, tunable textures with feature sizes less than 100 nm using these methods remains challenging. Block-copolymer-based thin-film patterning[24–27] can provide a potential solution because of its high spatial resolution and large area (>cm^2) throughput. Nanopillar arrays with ca. 100 nm period patterned by block-copolymer-micelle lithography have previously exhibited high water repellency (static water contact angle ≈ 150°).[28] However, to our knowledge, textures exhibiting both SH behavior and feature spacing less than 100 nm have not been demonstrated using this approach.

Here, we use block-copolymer-based thin-film patterning to create large-area SH surfaces textured with feature sizes approaching 10 nm. We show that tuning the nanostructure shape and aspect ratio dramatically influences the surface-wetting properties, with proper control crucial for achieving superhydrophobicity. In particular, SH behavior is obtained with a tapered-cone geometry but not a cylindrical pillar geometry. We assess the extreme robustness of the SH state using high-speed imaging of water droplets impacting these nanotextured surfaces. Our results support the conjecture that hierarchical roughness is not strictly necessary for achieving highly stable SH behavior. Furthermore, we demonstrate that our method allows fabrication of hierarchical surfaces when combined with conventional lithography, with potential applications in micro- and nano-fluidic devices.

We combine block-copolymer self assembly with plasma-based etching in order to generate nanostructured superhydrophobic surfaces over arbitrarily large areas. Block-copolymer thin films have found good application as non-lithographic patterning materials for fabricating magnetic nanostructures,[29–31]

Dr. A. Checco
Condensed Matter Physics
and Materials Science Department
Brookhaven National Laboratory
Upton, NY, 11973, USA
E-mail: checco@bnl.gov
Dr. A. Rahman, Dr. C. T. Black
Center for Functional Nanomaterials
Brookhaven National Laboratory
Upton, NY, 11973, USA
E-mail: ctblack@bnl.gov

DOI: 10.1002/adma.201304006

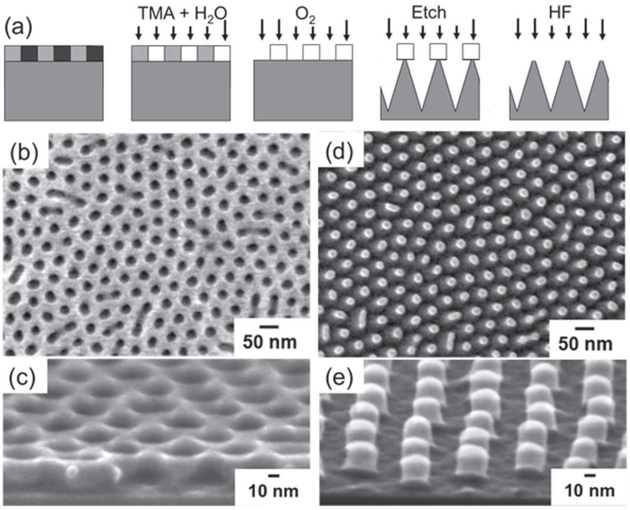

Figure 1. a) Schematic side views of process flow for creating a nanotextured surface from a self-assembled block-copolymer thin film. b) Top down and c) side-view scanning electron microscopy images of self-assembled cylindrical phase PS-*b*-PMMA block-copolymer film. Cylindrical PMMA domains have been chemically removed to improve imaging contrast. d) Top down and e) side-view SEM images of aluminum oxide nanostructures formed by block selective synthesis within self-assembled PMMA domains.

optical elements,[32,33] membranes,[28,34–36] and microelectronic device structures.[27,37] Our process begins by spin-casting a polystyrene-*block*-poly(methyl methacrylate) (PS-*b*-PMMA) block-copolymer thin film onto a flat silicon surface (1 wt% PS-*b*-PMMA in toluene, spun at 3000 rpm). Thermally annealing the sample (12 h, 200 °C in vacuum) facilitates block-copolymer self assembly via microphase separation, resulting in spontaneous formation of a film composed of uniform diameter PMMA cylindrical domains locally arranged in a close-packed hexagonal lattice (**Figure 1**a–c). The self-assembled domain size scales with the copolymer molecular weight. Here, we generate and compare nanostructured surfaces from block-copolymer templates having 25 nm features separated by 52 nm, and smaller 14 nm cylindrical domains (spaced by ca. 30 nm) formed from a lower-molecular-weight material. Suitable pretreatment of the silicon surface prior to block-copolymer film formation ensures that cylindrical PMMA domains orient perpendicularly.[31,38]

We render self-assembled block-copolymer thin films suitable for pattern transfer by selectively removing material from regions occupied by the PS block. Prior to PS removal, we subject samples to a sequence of three cycles of tri-methyl aluminum (TMA) and water vapor exposure, which incorporates aluminum oxide selectively into the PMMA domains by a process often termed sequential infiltration synthesis.[39–42] Subsequent removal of all the organic material from the film surface by oxygen-plasma etching leaves the silicon surface covered with close-packed, pill-shaped aluminum oxide nanostructures, with dimensions approximately reflecting the size of the self-assembled PMMA domains (e.g., 25 nm diameter, ca. 20 nm tall in Figures 1d,e).

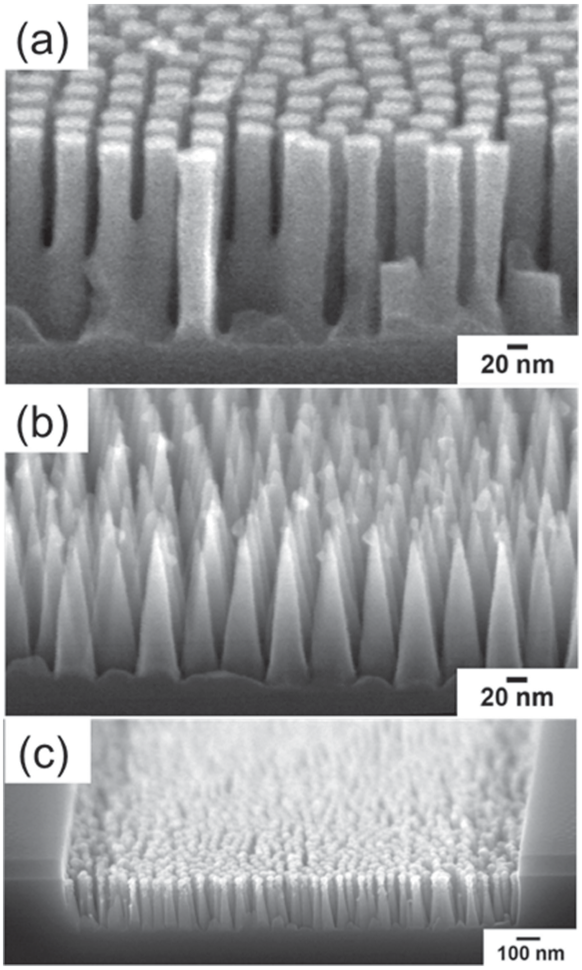

Figure 2. a) Side-view SEM image of a silicon surface textured with cylindrical pillars. b) Side-view SEM image of a silicon surface textured with nanocones. c) Side-view SEM image of nanocone surface formed in a select substrate area.

These aluminum oxide nanostructures provide a robust mask for nanotexturing the underlying silicon by plasma etching.[43] For example, we create surfaces covered with cylindrical pillars by anisotropically etching the silicon substrate using a sulfur hexafluoride:oxygen (SF_6:O_2) gas chemistry at low temperature (–100 °C).[44] Optimal etch conditions produce a nearly vertical sidewall, with pillar diameter and spacing determined by the block-copolymer template and pillar height dictated by etch time (**Figure 2**a). The surface shown in Figure 2a has a pillar density of ca. 10^{11} cm^{-2}, with average pillar radius of $r = 15$ nm and $h = 180$ nm. We removed any remaining alumina by briefly submersing the sample in dilute buffered hydrofluoric acid (50:1).

We can precisely tailor the surface nanotexture geometry by adjusting the silicon plasma etch process. For example, etching the silicon surface using a hydrogen bromide:chlorine:oxygen (HBr:Cl_2:O_2) chemistry produces a tapered sidewall profile[41] (Figure 2b) because these conditions introduce a slow lateral Si etch rate. The resulting conical nanostructures taper

DOI: 10.1002/adma.201304006

to a dimension ≤10nm at their tips – smaller than the initial self-assembled domain diameter. The nanostructure density remains fixed by the domain spacing of the PS-*b*-PMMA template.

We rendered the nanostructured silicon surfaces hydrophobic by passivating with a 2.5 nm thick octadecyltrichlorosilane (OTS) monolayer (immersion in 5 mm solution of OTS molecules in bicyclohexyl for 10 h) after first cleaning in piranha solution (3:1 volume ratio of sulfuric acid and hydrogen peroxide). We verified that the OTS coating does not significantly alter the surface topography by comparing SEM images of the surfaces before and after silanization.

In order to understand the effect of the nanotexture geometry, aspect ratio, and spacing on macroscopic wetting behavior, we fabricated surfaces decorated with either nanopillars or tapered cones with different height and spacing (dimensions summarized in **Table 1**). We estimated the hydrophobicity of flat and nanotextured surfaces by measuring the advancing contact angle and hysteresis of millimeter-sized, sessile water droplets. Nanotexturing dramatically enhances the hydrophobicity of both pillars and tapered cones, compared with chemically identical flat samples (Table 1). However, the quantitative behavior depends strongly on the nanotexture's shape. While the nanopillar texture increases the contact angle to as high as 150°, it also increases the contact angle hysteresis to 30°, irrespective of pillar height and spacing differences (Table 1). Previous experiments texturing surfaces with a block-copolymer-micelle approach have also reported advancing contact angles as large as ca. 150° on nanopillared surfaces with ca. 100 nm periodicity, without reporting the hysteresis.[28] In contrast, all the tapered cone surfaces investigated here exhibit SH behavior, having advancing angles exceeding ca. 160° and contact angle hysteresis smaller than 10°. These results demonstrate that identical texture spacings and heights can have dramatically different wetting behavior due to only the texture's geometry (within the range of sizes we investigated).

We understand our data using the CB model, in which a drop of water resting on a nanotextured surface makes contact only with the top of the textures without significantly penetrating into the structures. Indeed, our results show that, for identical feature geometry and spacing, the contact angle is independent of the feature height (Table 1). This picture is consistent with our earlier study on water penetration into deep hydrophobic cavities[23] where we found that the liquid infiltrates only a few nm into the structure. Under these conditions, the morphology of the texture top surface and the feature density determine the area fraction of solid in contact with the liquid, denoted as ϕ_{SL}. For a hexagonal array of pillars:

$$\varphi_{SL} \approx \frac{2\pi r^2}{d^2\sqrt{3}} \tag{1}$$

where r is the radius of the cylindrical pillar and d the pillar spacing. Substituting the geometrical parameters in Table 1 using the average nanopillar radius, $r \approx 15$ nm for 52 nm spaced pillars and $r \approx 10$ nm for 30 nm spaced pillars (Table 1, measured from SEM images), we obtain $\phi_{SL} = 30\%$ and $\phi_{SL} = 40\%$, respectively. The CB angle is given by:

$$\cos\theta_{CB} = \varphi_{SL}\,(\cos\theta_F + 1) - 1 \tag{2}$$

yielding $\theta_{CB} = 144°$ for 52 nm spaced pillars and $\theta_{CB} = 138°$ for 30 nm spaced pillars, in good agreement with the measured values of 150° and 137° to within 4% and 1%, respectively. We rationalize the large hysteresis measured on nanopillared surfaces following an argument made originally by Patankar et al.[45] As the contact line recedes on the textured surface, it may get pinned to the nanotexture, leaving behind a liquid layer on the pillars flat tops instead of a perfectly dry substrate. In a previous study, we have shown that water penetrates a few nanometers inside nanoscale cavities due to capillary effects and the cavity geometry. We expect the same phenomenon occurs here, with water slightly penetrating the voids between nanopillars favored by the rounded edges of the nanopillar's top. This may provide the mechanism for the pinning. Under these assumptions, the receding angle is provided by:[45]

$$\cos\theta_R = 2\varphi_{SL} - 1 \tag{3}$$

yielding $\theta_R = 114°$ for 52 nm spaced pillars and $\theta_R = 102°$ for 30 nm spaced pillars, which is similar to the measured receding contact angle of 120° and 110°, respectively.

We can similarly estimate the solid-liquid fraction for the tapered cone surfaces using Equation 1 by replacing the nanopillar radius with the typical curvature radius of the nanocone's tip, $r \approx 5$ nm (similar for both the 52 nm and 30 nm spaced cones). We obtain $\phi_{SL} = 4\%$ and $\theta_{CB} = 168°$, for the 52 nm spaced cones, and $\phi_{SL} = 10\%$ and $\theta_{CB} = 160°$ for the 30 nm spaced cones, in good agreement with the experimental values in the range 162–165°. The receding contact angle for the nanocone surfaces estimated using Equation 3 is 157° for the 52 nm spaced cones, and 143° for the 30 nm spaced cones, which is also comparable to the measured values of 160° and 155°, respectively.

A significant advantage of our block-copolymer self-assembly based patterning is its facile integration with thin-film fabrication methods. For example, we may combine this process with conventional photolithographic patterning in order to create surface nanotextures only within selected areas of a substrate. This is demonstrated in Figure 2c in which the bottom of a photolithographically defined, micrometer-wide, trench has been decorated with a tapered cone nanotexture using the same process described above for large-area surfaces. These hierarchical structures have applications, for example, as tailored,

Table 1. Average feature spacing, feature height, advancing water contact angle, and hysteresis of nanopatterned surfaces described in the main text.

Surface Texture	Spacing (±1 nm) [nm]	Feature height (±5 nm) [nm]	θ_{adv} (±2°) [°]	$\Delta\theta$ (±3°) [°]
Flat	NA	NA	112	6
52 nm spaced pillars	52	180	150	30
30 nm spaced pillars	30	75	137	27
52 nm spaced cones 1	52	75	165	5
52 nm spaced cones 2	52	180	165	6
30 nm spaced cones	30	95	162	7

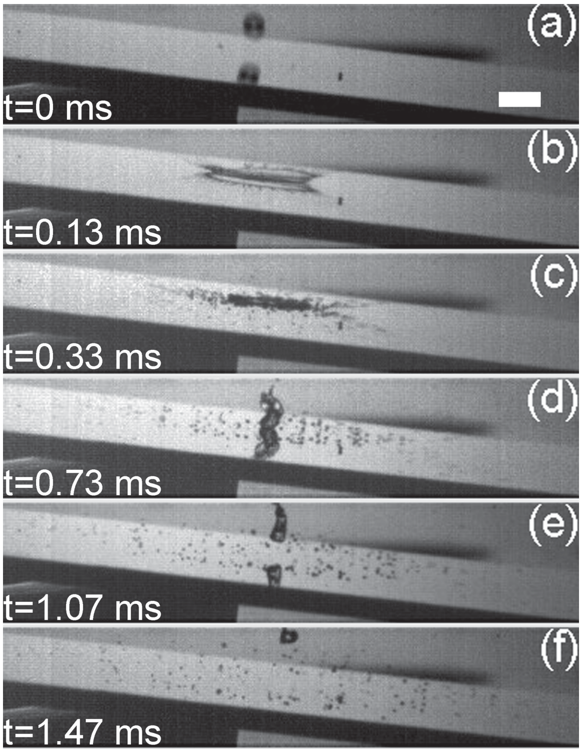

Figure 3. a–f) Temporal image sequence of a water drop (speed v = 10 m s^{-1}) impacting a surface nanopatterned with tapered cones texture (scale bar is 1 mm).

biomimetic SH surfaces or as microfluidic channels with self-cleaning and low fluid-friction properties.[22]

We investigated the robustness of the tapered-cone nanotexture surfaces by means of water droplet impingement experiments. We used a pressurized syringe and a narrow needle (0.13 mm internal diameter) to produce a spray of water droplets ranging in size from 0.3 to 2 mm. We aimed the spray at the patterned substrates with the needle positioned 0.75 m above the sample. The impact of the droplet on a textured surface was captured using a high-speed camera (Photron SA3), recording at a frame rate of 3 × 10^4 s^{-1}. In a representative splashing sequence (**Figure 3**), a water droplet (diameter = 0.5 mm) impacts a slightly tilted textured surface (tilt angle ≈ 6°) at a speed $V_0 = 10 \pm 1$ m s^{-1}, which we estimate from camera frames immediately preceding the impact (see Figure 3a). The surface texture consisted of tapered cones with 52 nm average spacing and 75 nm average height. Because of its speed and the surface superhydrophobicity, the droplet undergoes splashing[46] with the formation of a corona with a thickened, undulated rim (see Figure 3b). Subsequently, satellite droplets eject from the rim, while the central portion of the drop flattens out (see Figure 3c). The drop remnant recoils and bounces off the surface (Figure 3d), while the satellite drops spread radially outward from the impact zone (Figures 3e,f). We do not observe any pinned drops at the impact point after the drop has bounced back, to within the optical resolution of our measurement (ca: 50 µm), indicating that the surface remains in the CB state during the impact. We measure similar results for the other tapered cone surfaces described in Table 1.

We understand these findings by comparing the infiltration pressure generated during droplet impact with the static capillary pressure required to infiltrate the nanostructures. Immediately after impact, a "water hammer pressure" is generated due to the compression of liquid behind the shock wave. This pressure can be approximated as:[13]

$$P_{\mathrm{WH}} \approx 0.2 \rho c V_0 \tag{4}$$

where ρ is the liquid density and c is the speed of sound in the liquid. In our experiment, the droplet impact generates a pressure of $P_{\mathrm{WH}} \approx 3$ MPa on the nanostructure. As the droplet contact line expands and its speed decreases, the pressure drops to the incompressible dynamic pressure provided by the Bernoulli equation:[8,13]

$$P_{\mathrm{B}} = \frac{\rho}{2} V_0^2 \tag{5}$$

which for our experiments is $P_{\mathrm{B}} \approx 50$ kPa.

We can estimate the initial pressure (P_{C}) required to force the liquid/air interface inside the tapered cone nanostructure by balancing capillary and hydrostatic forces:[47]

$$P_{\mathrm{C}} = \frac{4\pi \gamma r \cos(\theta - \alpha)}{\sqrt{3}d^2 - 2\pi r^2} \tag{6}$$

where $\gamma = 7.2 \times 10^{-2}$ N m^{-1} is the water surface tension, $2\alpha \approx 20°$ is the opening angle of the tapered cones, and r the curvature radius of the three phase contact line wetting the cone's sidewall. Substituting $r \approx 5$ nm for the curvature radius of the cone's tip, we obtain $P_{\mathrm{C}} \approx 0.2$ MPa, which is smaller than P_{WH} and suggests that liquid penetrates the nanotexture upon droplet impact. However, the tapered cone geometry increases the required infiltration pressure as the liquid penetrates further into the texture (as shown by Equation 6). As the penetration depth increases, so does the length of the contact line (and therefore r) whereas the surface area of the liquid/air interface decreases, thereby raising P_{C}. From Equation 6, we estimate that ca. 1 MPa is required to infiltrate 50% of the nanotexture volume, with ca. 5 MPa necessary for 95% infiltration. The tapered cone textures with 30 nm spacing are even more robust. A pressure of ca. 0.7 MPa is required to initiate infiltration and ca. 2 MPa to infiltrate 50% of nanotexture volume. These considerations may explain the observed absence of droplet pinning after rebound for all tapered cones surfaces investigated here, for impact speeds as high as 10 m s^{-1}, which is the limit of our current experimental setup. A comprehensive, quantitative study of the ultimate robustness of these nanotextured surfaces will be a subject of our future investigation.

We have described a novel, block-copolymer-based fabrication approach for creating robust water repellent surfaces with well-defined textures at the 10 nm scale. A tapered cone geometry provides optimal SH behavior with large static water contact angles, low hysteresis, and resilience to water infiltration under high pressure. The flexibility of our patterning process is suitable for defining more complex geometries such as re-entrant textures, which are required to achieve repellence for

DOI: 10.1002/adma.201304006

both water and low surface tension liquids.[48] This fabrication approach expands the viability of superhydrophobic coatings for applications where extreme robustness and miniaturization are critical requirements. The precision and tunability with which nanotextures can be defined will facilitate fundamental studies of nanoscale aspects of superhydrophobicity.

Experimental Section

PS-b-PMMA Thin-Film Preparation: Cylindrical phase polystyrene-*block*-poly(methyl methacrylate) (PS-*b*-PMMA) block copolymers (Polymer Source, Inc.) with molecular weights of M_w = 99 kg/mol (PS:PMMA 64:35, polydispersity, PD = 1.09) and 48 kg/mol (PS:PMMA 31:17, PD = 1.06) were mixed at 1 wt% in toluene. Thin films were spin-cast at 3000 rpm for 45 s from solution onto silicon wafers and annealed in vacuum (<1 Torr) at 200 °C for 12 h. Prior to spin-coating the block copolymer, substrates were coated with a PS-*r*-PMMA random copolymer brush ($M_w \approx$ 11 kg/mol, PS:PMMA 52:48) by spin-casting (0.5 wt% in toluene, 600 rpm), thermal annealing for 4 h, and rinsing in toluene.

PS-*b*-PMMA templates were converted to aluminum oxide nanostructures by three sequential exposures to tri-methyl aluminum (TMA) (300 s, >5 Torr) and water vapor (300 s, >5 Torr) at 85 °C in a commercial atomic-layer-deposition system (Cambridge Nanotech Savannah S100). Remaining organic material was removed by oxygen plasma (20 W rf power, 100 mTorr) for 2 min (March Plasma CS1701).

Reactive Ion Etching: Reactive ion etching of structures with a cone profile was performed using an Oxford Instrument Plasma Lab 100 with a 50:50:10 ratio of HBr, Cl_2 and O_2 gas (10 mTorr, 60 W rf power, 250 W ICP) at room temperature. The process included a brief breakthrough step using BCl_3 and Cl_2 (20:5 sccm, 10 mTorr, 100 W rf power, 800 W ICP power) for 10 s in order to uniformly initiate silicon etching.

Reactive ion etching of structures with a pillar profile used a 40:50 combination of SF_6 and O_2 gas at −100 °C (12 mTorr, 15 W rf power, 800 W ICP). This process included a breakthrough step using SF_6:O_2 (40:50 sccm, 12 mTorr, 40 W rf power, 800 W ICP power) for 10 s.

Remaining Al_2O_3 was removed using buffered hydrofluoric acid (50:1) for 30 s. Samples were characterized by scanning electron microscopy (Hitachi S4800) operating at 20 kV.

Wetting Measurements: Contact angles of Millipore water droplets on passivated silicon surfaces were measured using a Dataphysics model OCA 15+ goniometer. Advancing (receding) angles were measured by slightly increasing (decreasing) the volume of the droplet (radius = 1 mm) with a motorized syringe with its needle immersed in the droplet.

Acknowledgements

This research was supported by the U.S. Department of Energy, Basic Energy Sciences in the Materials Sciences and Engineering Division (A. C.) and at the Center for Functional Nanomaterials (A.R. and C.B.) under Contract No. DE AC02 98CH10886. The authors acknowledge Dr. M. Diwan for kindly providing the high-speed camera.

Received: August 8, 2013
Revised: August 29, 2013

---

[1] W. Barthlott, C. Neinhuis, *Planta* **1997**, *202*, 1.
[2] X. F. Gao, L. Jiang, *Nature* **2004**, *432*, 36.
[3] K. Autumn, Y. A. Liang, S. T. Hsieh, W. Zesch, W. P. Chan, T. W. Kenny, R. Fearing, R. J. Full, *Nature* **2000**, *405*, 681.
[4] M. Callies, D. Quere, *Soft Matter* **2005**, *1*, 55.
[5] A. Marmur, *Langmuir* **2003**, *19*, 8343.
[6] M. Nosonovsky, *Langmuir* **2007**, *23*, 9919.
[7] A. B. D. Cassie, S. Baxter, *Trans. Faraday Soc.* **1944**, *40*, 546.
[8] M. Reyssat, A. Pépin, F. Marty, Y. Chen, D. Quéré, *Europhys. Lett.* **2006**, *74*, 306.
[9] M. Reyssat, J. M. Yeomans, D. Quéré, *Europhys. Lett.* **2008**, *81*, 26006.
[10] D. Bartolo, F. Bouamrirene, E. Verneuil, A. Buguin, P. Silberzan, S. Moulinet, *Europhys. Lett.* **2006**, *74*, 299.
[11] M. Nosonovsky, B. Bhushan, *Langmuir* **2007**, *24*, 1525.
[12] P. Papadopoulos, L. Mammen, X. Deng, D. Vollmer, H. J. Butt, *Proc. Natl. Acad. Sci. USA* **2013**, *110*, 3254.
[13] T. Deng, K. K. Varanasi, M. Hsu, N. Bhate, C. Keimel, J. Stein, M. Blohm, *Appl. Phys. Lett.* **2009**, *94*, 133109.
[14] M. Nosonovsky, B. Bhushan, *J. Phys.: Condens. Matter* **2008**, *20*, 395005.
[15] M. Nosonovsky, *Langmuir* **2007**, *23*, 3157.
[16] L. Gao, T. J. McCarthy, *Langmuir* **2006**, *22*, 2966.
[17] P. Kim, M. J. Kreder, J. Alvarenga, J. Aizenberg, *Nano Lett.* **2013**, *13*, 1793.
[18] M. McCarthy, K. Gerasopoulos, R. Enright, J. N. Culver, R. Ghodssi, E. N. Wang, *Appl. Phys. Lett.* **2012**, *100*, 263701.
[19] K. K. S. Lau, J. Bico, K. B. K. Teo, M. Chhowalla, G. A. J. Amaratunga, W. I. Milne, G. H. McKinley, K. K. Gleason, *Nano Lett.* **2003**, *3*, 1701.
[20] S. J. Cho, T. An, J. Y. Kim, J. Sung, G. Lim, *Chem. Commun.* **2011**, *47*, 6108.
[21] K.-C. Park, H. J. Choi, C.-H. Chang, R. E. Cohen, G. H. McKinley, G. Barbastathis, *ACS Nano* **2012**, *6*, 3789.
[22] K. Mawatari, S. Kubota, Y. Xu, C. Priest, R. Sedev, J. Ralston, T. Kitamori, *Anal. Chem.* **2012**, *84*, 10812.
[23] A. Checco, T. Hofmann, E. DiMasi, C. T. Black, B. M. Ocko, *Nano Lett.* **2010**, *10*, 1354.
[24] H.-C. Kim, S.-M. Park, W. D. Hinsberg, *Chem. Rev.* **2009**, *110*, 146.
[25] R. A. Segalman, *Mater. Sci. Eng. R: Rep.* **2005**, *48*, 191.
[26] J. Bang, U. Jeong, D. Y. Ryu, T. P. Russell, C. J. Hawker, *Adv. Mater.* **2009**, *21*, 4769.
[27] C. T. Black, R. Ruiz, G. Breyta, J. Y. Cheng, M. E. Colburn, K. W. Guarini, H. C. Kim, Y. Zhang, *IBM J. Res. Dev.* **2007**, *51*, 605.
[28] S. Krishnamoorthy, Y. Gerbig, C. Hibert, R. Pugin, C. Hinderling, J. Brugger, H. Heinzelmann, *Nanotechnology* **2008**, *19*, 285301.
[29] J. Y. Cheng, W. Jung, C. Ross, *Phys. Rev. B* **2004**, *70*, 064417.
[30] O. Hellwig, J. K. Bosworth, E. Dobisz, D. Kercher, T. Hauet, G. Zeltzer, J. D. Risner-Jamtgaard, D. Yaney, R. Ruiz, *Appl. Phys. Lett.* **2010**, *96*, 052511.
[31] T. Thurn-Albrecht, J. Schotter, C. Kastle, N. Emley, T. Shibauchi, L. Krusin-Elbaum, K. Guarini, C. Black, M. Tuominen, T. Russell, *Science* **2000**, *290*, 2126.
[32] D. H. Kim, K. H. A. Lau, J. W. F. Robertson, O. J. Lee, U. Jeong, J. I. Lee, C. J. Hawker, T. P. Russell, J. K. Kim, W. Knoll, *Adv. Mater.* **2005**, *17*, 2442.
[33] J. Yoon, W. Lee, E. L. Thomas, *Nano Lett.* **2006**, *6*, 2211.
[34] C. Black, K. Guarini, G. Breyta, M. Colburn, R. Ruiz, R. Sandstrom, E. Sikorski, Y. Zhang, *J. Vac. Sci. Technol. B* **2006**, *24*, 3188.
[35] W. A. Phillip, B. O'Neill, M. Rodwogin, M. A. Hillmyer, E. L. Cussler, *ACS Appl. Mater. Interfaces* **2010**, *2*, 847.
[36] S. Y. Yang, I. Ryu, H. Y. Kim, J. K. Kim, S. K. Jang, T. P. Russell, *Adv. Mater.* **2006**, *18*, 709.
[37] R. A. Farrell, N. T. Kinahan, S. Hansel, K. O. Stuen, N. Petkov, M. T. Shaw, L. E. West, V. Djara, R. J. Dunne, O. G. Varona, P. G. Gleeson, S. J. Jung, H. Y. Kim, M. M. Kolesnik, T. Lutz, C. P. Murray, J. D. Holmes, P. F. Nealey, G. S. Duesberg, V. Krstic, M. A. Morris, *Nanoscale* **2012**, *4*, 3228.

[38] P. Mansky, Y. Liu, E. Huang, T. Russell, C. Hawker, *Science* **1997**, *275*, 1458.

[39] J. Kamcev, D. S. Germack, D. Nykypanchuk, R. B. Grubbs, C.-Y. Nam, C. T. Black, *ACS Nano* **2012**, *7*, 339.

[40] Q. Peng, Y.-C. Tseng, S. B. Darling, J. W. Elam, *Adv. Mater.* **2010**, *22*, 5129.

[41] Q. Peng, Y.-C. Tseng, S. B. Darling, J. W. Elam, *ACS Nano* **2011**, *5*, 4600.

[42] M. Ramanathan, Y. C. Tseng, K. Ariga, S. B. Darling, *J. Mater. Chem. C* **2013**, *1*, 2080.

[43] Y. C. Tseng, Q. Peng, L. E. Ocola, J. W. Elam, S. B. Darling, *J. Phys. Chem. C* **2011**, *115*, 17725.

[44] D. E. Johnston, M. Lu, C. T. Black, *J. Micro/Nanolithography, MEMS, MOEMS* **2012**, *11*, 031306.

[45] N. A. Patankar, *Langmuir* **2003**, *19*, 1249.

[46] A. L. Yarin, *Annu. Rev. Fluid Mech.* **2006**, *38*, 159.

[47] E. J. Lobaton, T. R. Salamon, *J. Colloid Interface Sci.* **2007**, *314*, 184.

[48] A. Tuteja, W. Choi, J. M. Mabry, G. H. McKinley, R. E. Cohen, *Proc. Natl. Acad. Sci. USA* **2008**, *105*, 18200.

DOI: 10.1002/adma.201304006